Geoscience Letters

RESEARCH LETTER

Open Access

Retrieving ground displacements by tightly integrating inertial instruments with GNSS

S. W. Lee[1*], S. H. Yun[2], C. W. Chang[2*], J. R. Kim[3] and B. D. Tapley[1]

Abstract

Traditional methods for calculating near-field seismic displacements using the recordings of strong-motion accelerometers require a correction procedure to remove baseline offsets, which may result from ground rotation and tilting motions. However, the baseline correction is subjective and likely to remove low-frequency components of the seismic signals. We employ a new method based on the tightly coupled integration of accelerometers, gyroscopes and GNSS, which does not require the baseline correction. To investigate how well different retrieval methods account for the effects of the rotation and tilts on the displacements, synthetic case studies are conducted using the accelerometer recordings obtained from actual earthquakes. Results showed that the method employed can provide a clear improvement over the traditional methods when the accelerometer recordings are affected by the rotation and tilting motions of the ground. Additionally, the method effectively recovers permanent displacements, partly because it incorporates GNSS measurements that enable direct observation of the ground displacements and also partly because it avoids loss of information caused by the baseline correction.

Keywords Strong-motion accelerometers, Gyroscopes, GNSS, Tight coupling, Kalman filter, Tilts and torsion

Introduction

Accurate determination of near-source ground motion is important not only in understanding earthquake source mechanisms in seismological studies, but also improving building responses to strong ground motions in earthquake engineering (Hartzell and Heaton 1983; Wald and Heaton 1994; Kramer 1996; Takeo 1998; Symans et al. 1999; Igel et al 2005, 2007; Blewitt et al. 2009; Lee et al. 2009; Trifunac 2009; Ohta et al. 2012; Bernauer et al. 2014). The traditional approach to computing the displacements by doubly integrating accelerometer recordings require correction of baseline offsets in the recordings before the numerical integration, in which multiple steps of data processing such as detrending and high-pass filtering should be applied to obtain realistic displacements by removing the baseline offsets (Shakal et al. 2004). The offsets are known to be caused by various mechanisms including rotation and tilting motions of the ground or the instrumentation base, sensor hysteresis and ADC static buildup (Boore et al. 1980, 2003; Trifunac and Todorovska 2001; Emore et al. 2007). Such baseline correction is, however, a quite subjective process and it is not related closely to the physical mechanisms that generate the offsets. If correction parameters do not match well with characteristics of the baseline offsets of acceleration recordings, the correction may produce artifacts in resulting waveforms, which could be mistaken for actual seismic signatures. Also, for baseline-corrected acceleration records, a certain level of loss of seismic information is unavoidable, particularly for low-frequency or long-period signal, and as a result it is very difficult, if not impossible, to retrieve the permanent or residual

*Correspondence:
S. W. Lee
seungwoo.p.lee@gmail.com
C. W. Chang
iori@pusan.ac.kr
[1] Center for Space Research, University of Texas at Austin, Austin, TX 78759-5378, USA
[2] Volcano Specialized Research Center, Pusan National University, Busan, South Korea
[3] School of Aerospace and Mechanical Engineering, Korea Aerospace University, Goyang, South Korea

displacements accurately from the recordings (Graizer 2006).

For the tilt-induced baseline offsets, it seems more direct and physically meaningful to estimate the tilting and torsional motions of the ground together with translational motions of the ground and thus mitigate their effects on the ground displacements. Three-dimensional rotational motions of the ground can be sensed by a set of gyroscopes and like the strong-motion accelerometers, the gyroscope is an inertial sensor and requires numerical integration of angular rate recordings to compute rotations. Thus the sensor is subject to the same issue of accumulating errors with time as the strong-motion accelerometers, which results in unphysical, divergent signatures in the integrated signals and thus requires an analogous procedure to those used in correcting for the baseline offsets of the strong-motion accelerometers.

Such an issue is known to be addressed more effectively by complementing the inertial recordings by other independent measurements such as GNSS. Several attempts have been made to compute accurate ground displacements by combining the inertial instruments and GNSS based on complementary nature of these techniques. For example, Bock et al. (2011) used collocated GNSS receivers and accelerometers to compute both broadband (0 to tens of hertz) and precise ground displacement waveforms based on Kalman filter formulation. However, Bock et al. (2011) could not accommodate tilts and torsion of the accelerometers effectively and as a consequence had to heavily downweigh the accelerometer data in the integration with GNSS. The accuracy of the displacement waveforms computed by the proposed method was reported to be in the range of 0.8–1.0 mm in an RMS sense. The issue of tilts and torsion on strong-motion accelerometers was previously discussed by Graizer based on the equations of pendulum motion, in which the product of tilt angle and gravitational acceleration is shown to act as a forcing function to produce a response of horizontal accelerometers. It is noted that unlike the horizontal components the vertical recordings are less sensitive to the tilts (Graizer 2006).

The above studies are mostly based on shake table experiments to demonstrate their methods and one of the reasons for this is that there are few seismic stations which have collocated gyroscopes and GNSS receivers with strong-motion accelerometers. The displacement produced by the shake tables is generally limited to one-dimensional motion and it is difficult to generate realistic tilts and torsion using the shake tables. Also, these researchers used GNSS-derived positions for the integration instead of GNSS raw data. In the case that the GNSS position filter does not work properly for some reasons such as an insufficient number of available GNSS satellites, these integration methods fall back to produce purely inertial solutions that need to be corrected for baseline.

In this study we utilize GNSS raw measurements to optimally combine with 6-DOF (degree of freedom), i.e., three accelerometers and three gyroscopes data and investigate the performance of different methods to compute displacements when the sensors are subject to rotation and tilting motions during seismic events. Using the GNSS raw measurements for the integration has some advantages over using GNSS-derived position and listing a few, the measurement covariance can be computed more accurately when using the raw measurements and the integrated solution is provided even if the number of available GNSS satellites becomes less than four, which is the minimum required to compute position solutions using a single GNSS constellation. Due to the lack of collocated three-dimensional gyroscope recordings with associated GNSS and accelerometer data, we conduct synthetic case studies using the strong-motion accelerometer recordings obtained from actual seismic events such as El Mayor-Cucapah, Hector Mine and Northridge earthquakes. In principles, rotational motions can be represented in several interchangeable ways such as Euler angles, Direction Cosine Matrices (DCM), rotation vectors and quaternions and we utilize DCM (or equivalently rotation matrices) because it is quite intuitive and easy to manipulate.

This paper is organized as follows: in Sect. "Methods", we describe a method to synthesize the translational and rotational motions in the Earth-Centered Earth-Fixed (ECEF) reference frame, as well as a processing strategy to combine inertial and GNSS measurements based on the Extended Kalman Filter (EKF) formulation. Sect. "Results and discussion" presents results obtained by conducting a series of synthetic case studies where displacement waveforms are computed in different methods and compared with each other for the effectiveness. The methods include the traditional, double integration of accelerometer recordings and optimal combination of the three-sensor data using the EKF. We conclude by summarizing the findings and making suggestions for future research.

Methods

This section describes the method to generate three-dimensional strong-motion accelerometer and gyroscope data influenced by rotational and tilting motions of the ground as well as the basic formulation of the integration filter to optimally combine strong-motion accelerometer and gyroscope data with GNSS measurements. The physical layout of the sensors with associated coordinate systems is shown in Fig. 1. An ECEF

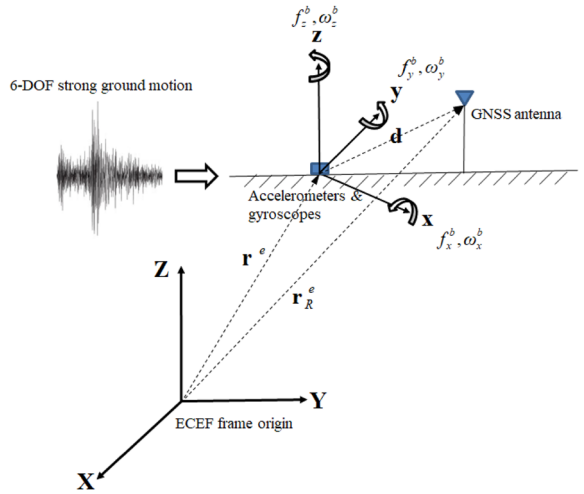

Fig. 1 A schematic showing the instrument layout and associated coordinate systems used in the formulation of the integration filter. The superscripts *e* and *b* denote the ECEF frame and the body frame, respectively. The origin of the body frame is where the strong-motion accelerometers and gyroscopes are installed and the sensitive axes of the strong-motion accelerometers are assumed to coincide with those of the gyroscopes

frame consisting of orthogonal XYZ axes serves as the reference frame for the formulation of the integration filter while a body frame is the frame to which the recordings from strong-motion accelerometers and gyroscopes are referenced, shown as the xyz triad in Fig. 1. The body frame is typically aligned with north, east and vertical directions. The origin of the body frame is denoted as $\mathbf{r}^e$ in the ECEF frame and the position of a GNSS antenna is given as $\mathbf{r}_R^e$ in ECEF. The difference between the two vectors is $\mathbf{d}$ that is usually expressed in the body frame.

In practice, accelerometer and gyroscope data are subject to various systematic and random errors. For given nominal values of specific force (nongravitational force per mass) $\mathbf{f}_{nominal}^b$ and angular rate $\boldsymbol{\omega}_{nominal}^b$ expressed in the body frame, the sensor outputs—contaminated by systematic and random errors such as biases, scaling factors, cross-coupling, and stochastic errors—can be modeled as follows:

$$\mathbf{f}_{meas}^b = (\mathbf{I}_3 + \mathbf{M}_a)\mathbf{f}_{nominal}^b + \mathbf{b}_a + \mathbf{w}_a,$$

$$\boldsymbol{\omega}_{meas}^b = (\mathbf{I}_3 + \mathbf{M}_g)\boldsymbol{\omega}_{nominal}^b + \mathbf{G}_g\mathbf{f}_{nominal}^b + \mathbf{b}_g + \mathbf{w}_g. \quad (1)$$

For the 6-DOF motions, $\mathbf{f}_{nominal}^b$, $\mathbf{f}_{meas}^b$, $\boldsymbol{\omega}_{nominal}^b$, $\boldsymbol{\omega}_{meas}^b$ are three-dimensional vectors. In Eq. (1), the subscripts *a* and *g* denote accelerometers and gyroscopes, respectively. $\boldsymbol{M}$ and $\boldsymbol{G}$ are 3×3 coefficient matrices which reflect the effects of scaling factors, cross coupling and gravity-dependence. $\boldsymbol{I}_3$ denotes a 3×3 identity matrix, and $\boldsymbol{b}$ and $\boldsymbol{w}$ are 3×1 vectors representing bias and random error, respectively. Each coefficient depends on the grades of accelerometers and gyroscopes and we use nominal values of the error PSD for navigation-grade accelerometers and gyroscopes and omit the bias and gravity-dependent effects. This may be translated in terms of precision as approximately 10^{-3} m/s^2 for the accelerometers and 10^{-7} rad/s for the gyroscopes. Table 1 summarizes the model coefficients for the 3-axis accelerometers and 3-axis gyroscopes used in this study and inserting $\mathbf{f}_{nominal}^b$ and $\boldsymbol{\omega}_{nominal}^b$ together with the coefficients into Eq. (1) yields accelerometer and gyroscope recordings in the body frame.

$$\mathbf{M}_i = \begin{bmatrix} m_{xx} & m_{xy} & m_{xz} \\ m_{yx} & m_{yy} & m_{yz} \\ m_{zx} & m_{zy} & m_{zz} \end{bmatrix}, \mathbf{w}_i = \begin{bmatrix} w_x \\ w_y \\ w_z \end{bmatrix}, \text{where } i = a, g.$$

In order to integrate GNSS measurements with the accelerometer and gyroscope data, it is necessary to represent these quantities in the ECEF frame as shown in Fig. 1. This can be accomplished by use of DCM or 3×3 orthonormal matrix $\mathbf{R}_b^e$ which transforms the vectors in the body frame to those in the ECEF frame as follows:

$$\boldsymbol{f}_{meas}^e = \boldsymbol{R}_b^e \boldsymbol{f}_{meas}^b,$$

Table 1 Model coefficients for the accelerometers and gyroscopes

	3-axis accelerometers	3-axis gyroscopes
Scaling factor (m_{xx}, m_{yy}, m_{xz})	(0.0002, − 0.0004, 0.00015)	(0.0001, − 0.0002, − 0.00015)
Cross-coupling (m_{xy}, m_{xz}, m_{yx}, m_{yz}, m_{zx}, m_{zy})	(− 0.0001, 0.00015, − 0.0005, 0.0001, − 0.00015, 0.0001)	(− 0.002, 0.0015, 0.0, 0.0001, 0.0, 0.0)
Random noise intensity (w_x, w_y, w_z)	(100.0, − 100.0, 300.0)×10^{-6}	(3.0, − 2.0, 5.0)×10^{-7}

Note that

$$\boldsymbol{R}_{b+}^{e+} = \boldsymbol{R}_{e-}^{e+}\boldsymbol{R}_{b-}^{e-}\boldsymbol{R}_{b+}^{b-}. \tag{2}$$

In Eq. (2), the superscript and subscript characters e and b denote the ECEF frame and the body frame, respectively. $\boldsymbol{R}_{b-}^{e-}$ and $\boldsymbol{R}_{b+}^{e+}$ are DCMs for body-to-ECEF transformation before and after temporal update, respectively, and $\boldsymbol{R}_{e-}^{e+}$ accounts for the Earth's rotation between time steps. The sampling interval for the accelerometer data can be used to set the time step, i.e., 0.005 s for 200 Hz sampling frequency. $\boldsymbol{R}_{b+}^{b-}$ represents temporal angular change of the body frame and is used to synthesize the effects of rotation and tilts of the ground. If rotation and tilting motions are given in terms of angular rate and the angular rate is approximately constant during sampling interval, $\boldsymbol{R}_{b+}^{b-}$ can be expressed as:

$$\boldsymbol{R}_{b+}^{b-} = \exp\left([\boldsymbol{\omega}_{meas}\times]\Delta t\right). \tag{3}$$

In Eq. (3), b denotes the body frame, and $\boldsymbol{\omega}_{meas}\times$ represents the skew symmetric matrix of angular rate measurement vector. Additionally, Δt is the sampling interval. Equation (3) is the exponential of integrated angular rate matrix and can be approximated using the Rodrigues' rotation formula [Dai 2015]. Using Eqs. (2) and (3), the effects of rotation and tilting of accelerometers on displacement waveforms can be simulated.

The accelerometer and gyroscope data can be combined with GNSS raw measurements to generate more accurate displacement waveform solutions, which belongs to a broader class of problems called sensor fusion or sensor integration (Durrant-Whyte 2016). Depending on what kind of GNSS data are used in the integration, the types of the integration can be divided into three: the loosely coupled integration if GNSS-derived positions are used as inputs for the fusion, tightly coupled integration for using GNSS raw data, and deeply coupled integration for using in-phase and quadrature data from the tracking loop of GNSS receivers (Greenspan et al. 1996; Jekeli 2000; Grewal et al. 2007; Farrell 2007). We employ the tightly coupled integration based on EKF formulation. The basic idea is that errors of inertially computed solutions consisting of displacement, velocity and tilts and torsion are estimated based on the differences between inertially predicted measurements and GNSS measurements and the estimated errors are fed back to correct the inertially computed solutions, which yields integrated solutions. For comprehensive description on the EKF formulation, readers are referred to Gelb (1974), Brown and Hwang (1997) and Tapley et al. (2004). Implementation of the tightly coupled integration using EKF is summarized as follows.

State variables for the tightly coupled integration can be divided into two: error states of the inertially computed solution and GNSS-related states. If the errors in position, velocity and tilts and torsion of the inertial solution are estimated, a partitioned state vector may be given as:

$$\mathbf{x} = \begin{bmatrix} \mathbf{x}_{IMU} \\ \mathbf{x}_{GNSS} \end{bmatrix}, \tag{4}$$

where.

$$\mathbf{x}_{IMU} = \begin{bmatrix} \delta\mathbf{r}^e \\ \delta\mathbf{v}^e \\ \delta\boldsymbol{\psi}^e \\ \mathbf{b}_a \\ \mathbf{b}_g \end{bmatrix} \text{and } \mathbf{x}_{GNSS} = \begin{bmatrix} \delta t_R \\ \delta\dot{t}_R \end{bmatrix}.$$

In Eq. (4), $\delta\mathbf{r}^e$, $\delta\mathbf{v}^e$, $\delta\boldsymbol{\psi}^e$ represent in sequence the position error, the velocity error, the tilts and torsion errors of the inertial solution expressed in the ECEF frame, respectively. $\mathbf{b}_a$ and $\mathbf{b}_g$ are baseline errors of the inertial instruments induced by mechanisms other than ground tilting motions. For the GNSS-related states, δt_R and $\delta\dot{t}_R$ denote the clock and frequency offsets of the GNSS receiver, respectively. Additional states like satellite-specific phase ambiguity can be included as well in $\mathbf{x}_{GNSS}$. Using the state-space formulation, temporal evolution of the state vector is given as a set of stochastic differential equations and the continuous, linearized system dynamics for the tightly coupled integration in the ECEF frame can be expressed in terms of system matrix $\mathbf{F}$ and zero-mean, Gaussian white noise $\mathbf{w}$[Wei and Schwarz 1990; Jekeli 2000; Rogers 2000]:

$$\dot{\mathbf{x}} = \mathbf{F}\mathbf{x} + \mathbf{w}, \tag{5}$$

where.

$$\mathbf{F} = \begin{bmatrix} 0 & \mathbf{I}_3 & 0 & 0 & 0 & 0 & 0 \\ -\frac{2\mathbf{g}^e}{r^e}\frac{\mathbf{r}^{eT}}{|r^e|} & -2\boldsymbol{\omega}_e\times & -\mathbf{R}_b^e\mathbf{f}_{meas}^b\times & \mathbf{R}_b^e & 0 & 0 & 0 \\ 0 & 0 & -\boldsymbol{\omega}_e\times & 0 & \mathbf{R}_b^e & 0 & 0 \\ 0 & 0 & 0 & 0 & 0 & 0 & 0 \\ 0 & 0 & 0 & 0 & 0 & 0 & 0 \\ 0 & 0 & 0 & 0 & 0 & 0 & 1 \\ 0 & 0 & 0 & 0 & 0 & 0 & 0 \end{bmatrix}.$$

As can be seen in Eq. (5), $\mathbf{F}$ is given as a function of $\mathbf{f}_{meas}^e$, $\mathbf{R}_b^e$ (Eq. (2)) and some other parameters such as the angular velocity vector of the Earth $\boldsymbol{\omega}_e$ and the acceleration due to gravity $\mathbf{g}^e$. To implement the EKF filter Eq. (5) needs to be discretized and the time update of the state vector and associated error covariance from kth epoch to $k+1$ th epoch is expressed by use of state transition matrix $\boldsymbol{\Phi}$ and process noise matrix $\mathbf{Q}_k$:

$$\begin{aligned} \mathbf{x}_{k+1} &= \boldsymbol{\Phi}(t_k, t_{k+1})\mathbf{x}_k + \mathbf{w}_k \\ \mathbf{P}_{k+1} &= \boldsymbol{\Phi}(t_k, t_{k+1})\mathbf{P}_k\boldsymbol{\Phi}^T(t_k, t_{k+1}) + \mathbf{Q}_k, \end{aligned} \tag{6}$$

where.

$$\mathbf{\Phi}(t_k, t_{k+1}) = \exp(\mathbf{F}\Delta t) \approx \mathbf{I} + \mathbf{F}\Delta t = \begin{bmatrix} 0 & \mathbf{I}_3\Delta t & 0 & 0 & 0 & 0 & 0 \\ -\frac{2\mathbf{g}^e}{r^e}\frac{\mathbf{r}^{eT}}{|r^e|}\Delta t & \mathbf{I}_3 - 2[\boldsymbol{\omega}_e\times]\Delta t & -\mathbf{R}_b^e[\mathbf{f}_{meas}^b\times]\Delta t & \mathbf{R}_b^e\Delta t & 0 & 0 & 0 \\ 0 & 0 & \mathbf{I}_3 - [\boldsymbol{\omega}_e\times]\Delta t & 0 & \mathbf{R}_b^e\Delta t & 0 & 0 \\ 0 & 0 & 0 & \mathbf{I}_3 & 0 & 0 & 0 \\ 0 & 0 & 0 & 0 & \mathbf{I}_3 & 0 & 0 \\ 0 & 0 & 0 & 0 & 0 & 1 & \Delta t \\ 0 & 0 & 0 & 0 & 0 & 0 & 1 \end{bmatrix}$$

and.

$$\mathbf{Q}_k = \mathbf{E}\left[\mathbf{w}_k^T\mathbf{w}_k\right] = \int_{t_k}^{t_{k+1}} \Phi(t_k,\tau)\,diag\left[\,\mathbf{q}_p\ \mathbf{q}_V\ \mathbf{q}_A\ \mathbf{q}_{ba}\ \mathbf{q}_{bg}\ q_{cp}\ q_{cf}\,\right]\Phi^T(t_k,\tau)d\tau.$$

In Eq. (6), $\mathbf{E}$ denotes the expectation operation and Δt is time difference between t_k and t_{k+1} and *diag* means diagonal entries for a square matrix whose off-diagonal entries are all zeroes. If $\Delta t \leq 1$ and the errors in the velocity of the inertial solution are driven by integrated random noise of the acceleration, $\mathbf{Q}_k$ may be approximated as:

$$\mathbf{Q}_K \approx \begin{bmatrix} \mathbf{Q}_{IMU} & \mathbf{0} \\ \mathbf{0} & \mathbf{Q}_{GNSS} \end{bmatrix}, \tag{7}$$

where.

$$\mathbf{Q}_{IMU} = diag\left[\,0\ \mathbf{q}_V\Delta t\ \mathbf{q}_A\Delta t\ \mathbf{q}_{ba}\Delta t\ \mathbf{q}_{bg}\Delta t\,\right],$$

$$\mathbf{Q}_{GNSS} = \begin{bmatrix} q_{cp}\Delta t + \frac{q_{cf}\Delta t^3}{3} & \frac{q_{cf}\Delta t^2}{2} \\ \frac{q_{cf}\Delta t^2}{2} & q_{cf}\Delta t \end{bmatrix}.$$

In Eq. (7), $\mathbf{q}_V$, $\mathbf{q}_A$, $\mathbf{q}_{ba}$ and $\mathbf{q}_{bg}$ denote noise intensity vectors of the strong-motion accelerometers, the gyroscopes, the accelerometer biases and the gyroscope biases, respectively. q_{cp} and q_{cf} represent noise intensity of clock phase and frequency of the GNSS receiver.

For measurement update of the tightly coupled integration EKF, we use ionosphere-free pseudorange ρ and Doppler measurement f_{Dop}, and the measurement dynamics for ρ and f_{Dop} can be expressed as follows:

$$\rho = \left(\boldsymbol{r}_S^e - \boldsymbol{r}_R^e\right) + \delta\rho + c\delta t_R,$$

$$f_{Dop} = \mathrm{d}\Phi/\mathrm{d}t = \frac{1}{\lambda}\left[\boldsymbol{u}_j^{eT}\left[\left(\boldsymbol{v}_S^e + \boldsymbol{\omega}_e \times \boldsymbol{r}_S^e\right) - \left(\boldsymbol{v}_R^e + \boldsymbol{\omega}_e \times \boldsymbol{r}_R^e\right)\right] + \delta\dot{\rho} + c\delta\dot{t}_R\right] \tag{8}$$

In Eq. (8), the subscripts S and R represent the satellites and the receiver, respectively. Φ denotes ionosphere-free carrier-phase measurements, while λ represents the effective wavelength of the ionosphere-free carrier-phase, and $\boldsymbol{u}_j^e$ refers to the unit vector aligned with the signal path between jth satellite and the receiver, respectively. Note that $\mathbf{r}_R^e$ and $\mathbf{v}_R^e$ are the position and velocity vectors of the receiver expressed in the ECEF frame and different from $\mathbf{r}^e$ and $\mathbf{v}^e$ in Eq. (4), which denotes the position and velocity vectors of the inertial instruments in the ECEF frame.

As shown in Eq. (8), we use the time derivative of carrier-phase measurements instead of the carrier-phase measurements themselves. The actual calculation of the Doppler frequency involves time-differencing carrier-phase measurements divided by a sampling interval (e.g., 1 s). Through this process, slowly varying and constant terms, such as phase ambiguity, are largely canceled out, greatly simplifying the filter formulation. For readers interested in using undifferenced carrier-phase measurements and handling the associated carrier-phase ambiguities, we refer them to Lee et al. (2013, 2015).

Other GNSS errors, such as tropospheric delay and antenna phase offsets for both the receiver and satellites, are omitted in this study because these errors are considered relatively constant given the time scale of seismic events, which typically last only a few minutes, and thus are largely mitigated by the time-differencing process. A similar assumption was made in Colosimo et al. (2011), where carrier-phase-based Doppler measurements—similar to our approach—used to compute centimeter-level coseismic deformations in real-time mode.

In addition to systematic errors, Gaussian noise is added to the measurements to ensure that GNSS-only position solutions achieve a similar level of accuracy to PPP solutions—approximately 1–3 cm in the horizontal components and 2 cm or more in the vertical. We

assume no relative motion between the inertial instruments and the GNSS antenna during seismic events. However, in practice, this assumption may not always hold. We discuss scenarios where relative motion between the GNSS and inertial sensors may occur, such as due to ground non-rigidity.

As shown in Fig. 1, $\mathbf{r}_R^e$ and $\mathbf{v}_R^e$ can be computed in terms of position difference vector $\mathbf{d}$ expressed in the body frame together with $\mathbf{r}^e$, $\mathbf{v}^e$ and other parameters given by Eqs. (1) and (2):

$$\begin{aligned}\mathbf{r}_R^e &= \mathbf{r}^e + \mathbf{R}_b^e\mathbf{d}\\ \mathbf{v}_R^e &= \mathbf{v}^e + \mathbf{R}_b^e(\boldsymbol{\omega}_{meas}\times\mathbf{d}) + \boldsymbol{\omega}_e\times\mathbf{R}_b^e\mathbf{d}.\end{aligned} \tag{9}$$

The linearized measurement dynamics for the tightly coupled integration is obtained by taking partial derivatives of the measurement dynamics $\mathbf{h}_k$(Eq. (8)), with respect to the state variables, which may be expressed as:

$$\mathbf{z}_k = \mathbf{H}_k\mathbf{x}_k + \boldsymbol{\nu}_k,\ \ \mathbf{H}_k = \frac{\partial\mathbf{h}_k}{\partial x}, \tag{10}$$

where.

$$\mathbf{z}_k = \begin{bmatrix} \rho_{meas,1} - \rho_{pred,1} \\ \vdots \\ \rho_{meas,M} - \rho_{pred,M} \\ f_{meas,1} - f_{pred,1} \\ \vdots \\ f_{meas,M} - f_{pred,M} \end{bmatrix},$$

$$\mathbf{H}_k = \begin{bmatrix} \mathbf{u}_1^e & 0 & 0\,0\,0\,1 & 0 \\ \vdots & \vdots & \vdots\,\vdots\,\vdots\,\vdots & \vdots \\ \mathbf{u}_M^e & 0 & 0\,0\,0\,1 & 0 \\ 0 & \mathbf{u}_1^e/\lambda & 0\,0\,0\,0 & 1/\lambda \\ \vdots & \vdots & \vdots\,\vdots\,\vdots\,\vdots & \vdots \\ 0 & \mathbf{u}_M^e/\lambda & 0\,0\,0\,0 & 1/\lambda \end{bmatrix},$$

$$\boldsymbol{\nu}_k = N(0,\mathbf{C}_k),\ \ \mathbf{C}_k = diag\left[\ \sigma_{\rho,1}^2\ \cdots\ \sigma_{\rho,M}^2\ \sigma_{f,1}^2\ \cdots\ \sigma_{f,M}^2\ \right].$$

In Eq. (10), M is the number of satellites available at kth epoch and $\mathbf{z}_k$ is the residual vector that is computed by subtracting predicted GNSS measurements using the inertial solutions from observed GNSS measurements. $\boldsymbol{\nu}_k$ represents zero-mean, Gaussian distributed measurement noise vector at kth epoch, whose covariance is a diagonal matrix $\mathbf{C}_k$. The diagonal entries of $\mathbf{C}_k$ are noise variances of the GNSS measurements. Using Eqs. (4) – (10), Eq. (11) implements the tightly coupled integration between strong-motion accelerometers, gyroscopes and GNSS based on the EKF formulation (Gelb 1974; Brown and Hwang 1997; Tapley et al. 2004):

$$\begin{aligned}\tilde{\mathbf{x}}_k &= \boldsymbol{\Phi}(t_k,t_{k-1})\hat{\mathbf{x}}_{k-1}\\ \tilde{\mathbf{P}}_k &= \boldsymbol{\Phi}(t_k,t_{k-1})\hat{\mathbf{P}}_{k-1}\boldsymbol{\Phi}^T(t_k,t_{k-1}) + \mathbf{Q}_k\\ \mathbf{K}_k &= \tilde{\mathbf{P}}_k\mathbf{H}^{\mathbf{T}}(\tilde{\mathbf{x}}_k)\left[\mathbf{H}(\tilde{\mathbf{x}}_k)\tilde{\mathbf{P}}_k\mathbf{H}^{\mathbf{T}}(\tilde{\mathbf{x}}_k) + \mathbf{C}_k\right]^{-1}.\\ \hat{\mathbf{x}}_k &= \tilde{\mathbf{x}}_k + \mathbf{K}_k[\mathbf{z}_k - \mathbf{h}_k(\tilde{\mathbf{x}}_k)]\\ \hat{\mathbf{P}}_k &= [\mathbf{I} - \mathbf{K}_k\mathbf{H}_k(\tilde{\mathbf{x}}_k)]\tilde{\mathbf{P}}_k\end{aligned} \tag{11}$$

As can be seen in Eq. (4), the integration filter is based on the error states of the inertial solutions and total states of the GNSS measurements and the error states estimated by the filter are fed back to form the total state of the integrated solutions and the error state is reinitialized to zero. Because of the return to zero of the error states after the measurement update phase of the EKF, the time update of the EKF is applied mainly to state error covariance, which simplifies the implementation.

In order to facilitate the convergence of the EKF, initial values of the tilts and torsion can be given by leveling and gyrocompassing during pre-event period, taking advantage of the fact that the only signal observed by stationary accelerometers is the reaction to Earth's gravity and by the similar reasoning, Earth's rotation by stationary gyroscopes (Rogers 2000; Titterton and Weston 2004). Accordingly initial estimates of eastward tilt φ, northward tilt θ and torsion ψ can be given in terms of the specific force and angular velocity measurements from the accelerometers and gyroscopes as follows:

$$\begin{bmatrix}\varphi\\ \theta\\ \psi\end{bmatrix} = \begin{bmatrix} \arctan 2\left(-f_y,-f_z\right) \\ \arctan\left(-f_x\Big/\sqrt{\left(f_y^2+f_z^2\right)}\right) \\ \arctan 2\left(-\omega_y\cos\varphi + \omega_z\sin\varphi,\ \omega_x\cos\theta + \omega_y\sin\varphi\sin\theta + \omega_z\cos\varphi\sin\theta\right)\end{bmatrix}. \tag{12}$$

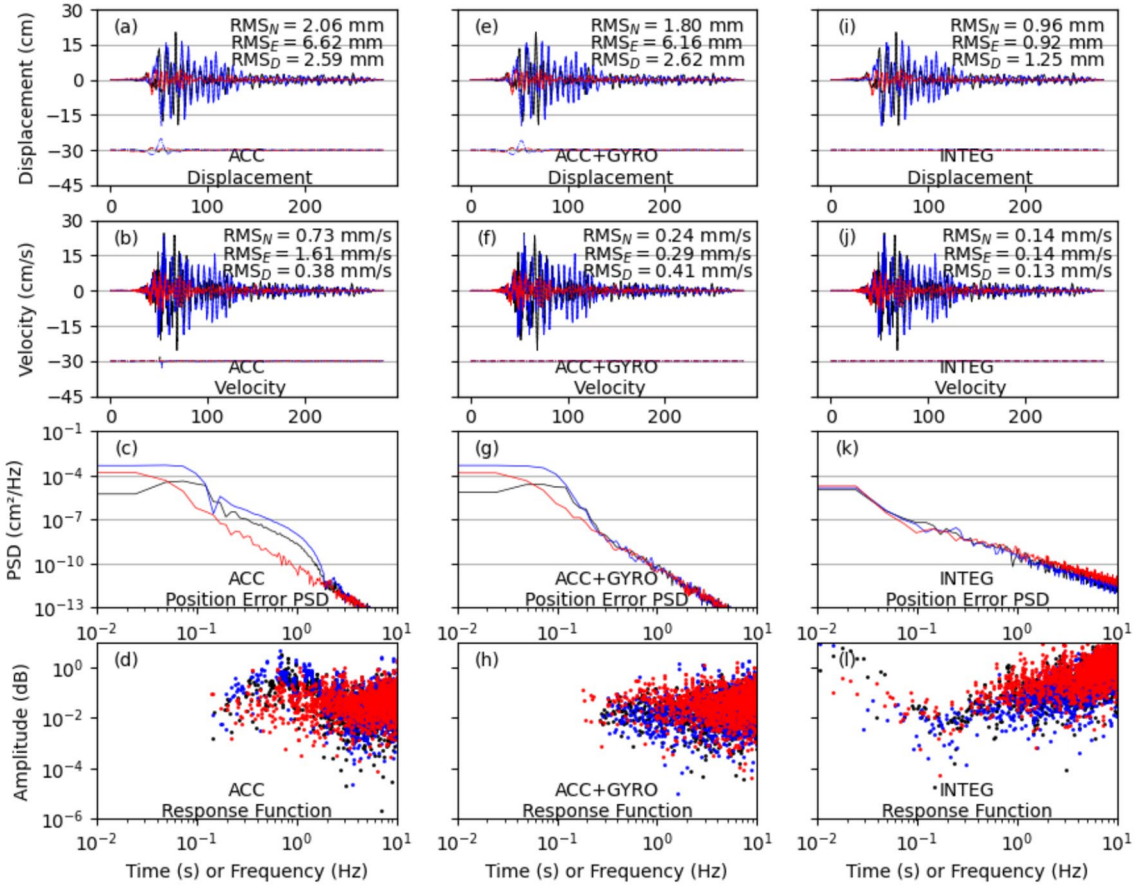

Fig. 2 Results obtained by processing the recordings of the El Mayor-Cucapah earthquake where sinusoidal rotation and tilts motions are applied to north (black), east (blue) and vertical (red) axes with no initial orientation errors (M1). Truth displacement and velocity waveforms are plotted as dashed lines with the same color as the corresponding solutions from the individual methods. The displacement and velocity differences between the solutions and truth waveforms are plotted as dash-dot lines and shifted downward by 30 cm for displacement and 30 cm/s for velocity to improve clarity. ACC denotes the solution computed from the strong-motion accelerometers only, ACC + GYRO denotes the solution from the inertial instruments (i.e., strong-motion accelerometers and gyroscopes) and INTEG denotes the solution obtained by tightly integrating GNSS with the inertial instruments. The subscripts N, E, and D represent north, east and vertical directions, respectively. **a**, **b**, **c** and **d** show displacements, velocities, PSD of position errors, and displacement response functions obtained by the ACC method, respectively. The definition of the response function is provided in the manuscript. Similarly, **e**, **f**, **g**, **h** for ACC + GYRO and **i**, **j**, **k**, **l** for INTEG. The INTEG method provides more accurate displacement and velocity waveforms than ACC and ACC + GYRO at least by 40%, particularly for horizontal components in displacement **i**and velocity (**j**). In **k** the PSD values of INTEG show a lower level of errors in the frequency band from 0.01 to 0.4 Hz compared to those of ACC and ACC + GYRO while the PSD is higher than those of the two in the frequency band above. Compared to the response functions of ACC **d** and ACC + GYRO **h**, the INTEG response function **l** spans broader frequency band, while showing greater values for the frequency band from 1 Hz and beyond. The noisier characteristic in the upper band seems to be the side effects of GNSS aiding

It is noted that the initial values of tilting angles can be determined reasonably accurately by the leveling from strong-motion accelerometer data only while for torsion, Earth's rotation is a weak signal and the values of torsion obtained from gyrocompassing are time-averaged to reduce noise.

Results and discussion

We conducted synthetic case studies by applying simulated rotation and tilting motions to actual accelerometer recordings. Three real earthquake events were analyzed: the 2010 Mw 7.2 El Mayor-Cucapah earthquake, the 1999 Mw 7.1 Hector Mine earthquake, and the 1994 Mw 6.7 Northridge earthquake.

For each event, we selected a station that provided uncalibrated accelerometer recordings initially aligned with the north, east, and up directions and remained stable throughout the event. Additionally, we prioritized stations where the maximum horizontal velocity was sufficiently high (e.g., at least 0.1 m/s) to generate velocity-dependent tilt errors detectable by gyroscope measurements. Beyond these criteria, no further restrictions were imposed on station selection. The selected stations are as follows:

- El Centro—Meloland Geotechnical Station for the El Mayor-Cucapah earthquake.
- San Bernardino—Fire Station #10 for the Hector Mine earthquake.
- Jensen Filter Plant Generator Building for the Northridge earthquake.

Firstly, three-dimensional accelerometer recordings from the El Centro—Meloland Geotechnic site for the 2010 Mw 7.2 El Mayor-Cucapah earthquake are processed, which span approximately 280 s and are sampled at the frequency of 200 Hz. Two different error models of tilts and torsion are used in the study, as follows:

- M1: No initial orientation errors and 1-s long, sinusoidal tilts and torsion applied at the time when peak velocities of the individual components occur. The amplitudes of the sinusoids are scaled to be 0.5, 0.3 and 0.1 degrees for eastward and northward tilts and torsion, respectively.
- M2: Initial misorientation of 0.7, 0.5 and 0.3 degrees for eastward and northward tilts and torsion applied, respectively, and time series of tilts and torsion applied, which are proportional to the velocity waveforms that correspond to each rotational axis and are scaled to have peak rotational displacements of 0.5, 0.3 and 0.1 degrees for eastward and northward tilts and torsion, respectively.

In the above models the angular errors may be divided into initial (or static) and coseismic (or dynamic) parts. For the initial angular errors, the accelerometers and gyroscopes are assumed to be perfectly aligned with local North-East-Down (NED) frame in M1 while in M2 the accelerometers are misaligned with the NED frame at the beginning. For the coseismic angular errors, the tilts and torsion errors have a single frequency component and last for 1 s in M1 while in M2 the errors occupy a band of frequency spectrum which has the same bandwidth as that of velocity signals. This is based on the previous works where the tilts and torsion were reported to be correlated with velocity profiles (Bouchon and Aki 1982; Trifunac 1982; Trifunac and Todorovska 2001).

The data generated with each model are processed separately by three different processing methods so as to examine their relative performance. The first one is the traditional method of numerically integrating accelerometer recordings twice and denoted hereafter by ACC. The second is the numerical integration of both accelerometer and gyroscope recordings (Nigbor 1994) and is denoted by ACC+GYRO. The third is to use the EKF-based tightly coupled integration technique described in the previous section and denoted by INTEG. Baseline corrections are applied to the results obtained with ACC and ACC+GYRO, where the velocity waveforms are detrended, highpass-filtered and integrated to generate corresponding displacement waveforms. Otherwise the integrated waveforms would produce unphysical drift in displacement, which results in significant displacement error. The detrending is conducted by fitting 14th-order polynomial to the velocity waveforms and the corner frequency of the high-pass filter is set to 0.05 Hz.

Figure 2 shows the results obtained by processing the M1 data with the three methods. Note that the truth displacement and velocity waveforms are plotted together with the individual solutions, which have the same color with the solutions but different line styles (dashed lines for truth and solid lines for solutions). In Figs. 2 and 3, the solution and truth waveforms may appear indistinguishable due to their close spacing. To enhance clarity, the difference waveforms between them are additionally plotted using a dash-dot line style and are shifted downward by 30 cm for displacement and 30 cm/s for velocity. Reviewing the truth velocity profiles indicates that the peak velocity occurs at the time of 52.5, 50.4 and 49.8 s for north, east and vertical components, respectively, and 1-Hz sinusoids of tilts and rotation are applied at those times. Displacement and velocity errors are obtained by computing the difference from the truth waveforms and comparing ACC and ACC+GYRO results, the velocities obtained with ACC+GYRO are found to be at least 20% more accurate than those with ACC while for displacements the differences in accuracy between ACC+GYRO and ACC are somewhat reduced compared to the velocities. Results obtained with INTEG show clear improvement over those of ACC and ACC+GYRO, particularly for horizontal components in displacement and velocity and quantitatively, the improvement in accuracy over those of ACC and ACC+GYRO is more than 40% in both displacement and velocity.

For the PSD of the ACC position differences, there exist prominent bulges in horizontal components spanning approximately from 0.15 Hz to 2 Hz. This seems to be the signature of the 1-Hz sinusoidal tilting motions smeared by the baseline correction process. This signature is not observed in the PSD plot of ACC+GYRO, which implies that the gyroscopes effectively account for the sinusoidal tilting motions. Also the vertical component of the PSD of the ACC solutions does not show such signature. The PSD values of INTEG show a lower level of errors in the frequency band from 0.01 to 0.4 Hz compared to that of ACC+GYRO while the PSD is higher in the frequency band above. The magnitude of displacement errors in the upper band is less than approximately 3.1×10^{-5} cm in all three components. Figure 2d, h, and l shows the amplitude spectra of the response functions for the individual

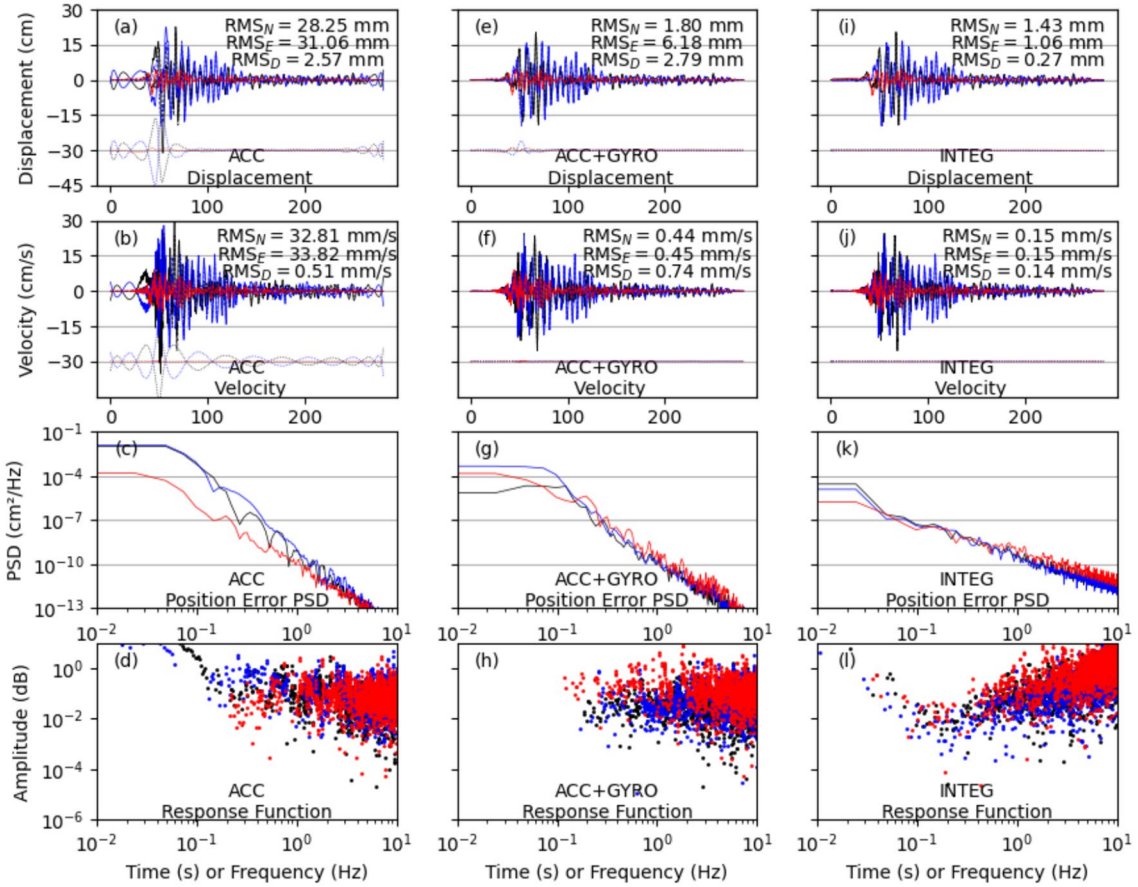

Fig. 3 Results obtained by processing the recordings of the El Mayor-Cucapah earthquake where profiles of rotation and tilts motions are applied with initial misorientation (M2). Readers are referred to Fig. 2 for the acronyms and symbols. Panels **a**, **b**, **c** and **d** show displacements, velocities, PSD of position errors, and displacement response functions obtained by the ACC method, respectively. Similarly, panels **e**, **f**, **g**, **h** correspond to the ACC + GYRO method, and panels **i**, **j**, **k**, **l** to the INTEG method. In a there are a few artifacts, including a prominent peak in north (black) displacement located at the time of approximately 55 s, which might be misinterpreted as real seismic signature. These artifacts may be attributed to the extension of the ACC response function and the amplification of the signal in frequencies below 0.1 Hz, as shown in **d**. For the ACC + GYRO solution, the displacement errors of horizontal and vertical components are approximately at the same level as the previous case while the RMS errors of velocity are increased in all three components. In **i** the INTEG displacements are shown to be more accurate than those of ACC and ACC + GYRO at least by 20%. In **k** the error PSD of vertical displacement of INTEG is somewhat increased in the frequency range near and above 1 Hz compared to the counterpart in Fig. 2. Similar to Fig. 2**l**, the INTEG response functions extend into the low frequency band, showing attenuation between 0.1 Hz and 1 Hz frequency band and amplification for high-frequency signals

displacement solutions. Here, the response function is defined as the ratio of the Fourier transform of the solution displacement to the Fourier transform of the truth displacement. This metric helps assess the fidelity of the solutions across different frequencies. Comparing the response functions in Fig. 2d, h and l, it can be observed that the frequency band occupied by the INTEG method extends into very low frequency band (i.e., < 0.1 Hz) while the bands of ACC and ACC + GYRO stop around 0.1 Hz. For the frequencies above 1 Hz, the magnitude of the INTEG response function is somewhat greater than 1, which indicates that the high-frequency noise could be amplified. The noisier characteristic in the upper band is likely due to the effects of GNSS corrections to the displacement waveforms. For the frequency band between 0.1 Hz to 1 Hz, the INTEG response function is somewhat lower than those of ACC and ACC + GYRO.

Similar to Fig. 2, results obtained with M2 are shown in Fig. 3. Compared with the previous results, the RMS errors of the ACC displacements are increased significantly in the horizontal components while the vertical RMS error is approximately the same. It can be observed in Fig. 3a that there are a few artifacts in ACC displacement waveforms, including the sinusoidal variations in north (black) and east (blue) displacements for the first tens of seconds, and a prominent peak in north displacement located at the time of approximately 55 s, which result in the increment of the RMS error of the ACC

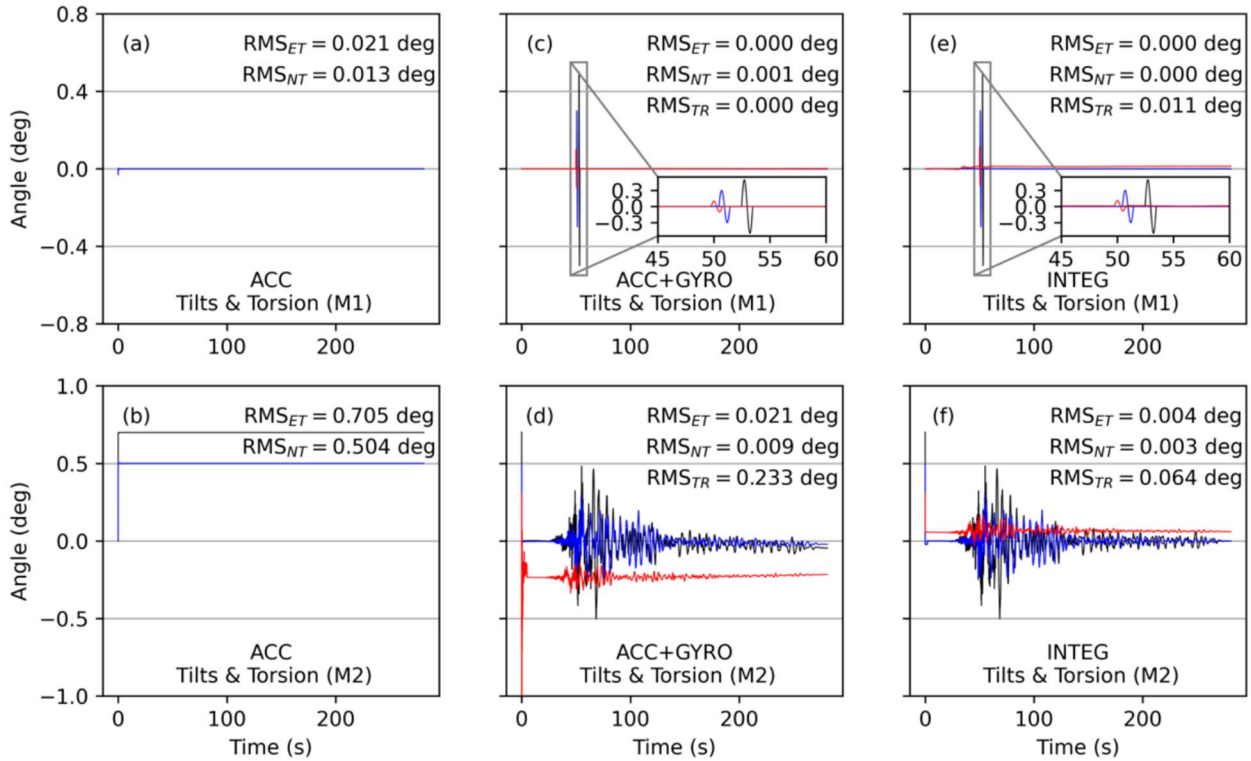

Fig. 4 Tilts and torsion profiles obtained by processing the recordings of the El Mayor-Cucapah earthquake without initial misorientation (M1, shown in upper panel) and with initial misorientation (M2, lower panel). Readers are referred to Fig. 2 for the acronyms and symbols. Panels **a**, **b**, **c** and **d** show displacements, velocities, PSD of position errors, and displacement response functions obtained by the ACC method, respectively. Similarly, panels **e**, **f**, **g**, **h** correspond to the ACC + GYRO method, and panels **i**, **j**, **k**, **l** to the INTEG method. The subscripts ET, NT, and TR denote eastward tilt, northward tilt and torsion, respectively. **a** and **b** show the tilts profiles of the ACC solutions for the M1 and M2 cases, respectively. These profiles are computed using Eq. (11), where the tilts are averaged for 5 s and held fixed afterward. Torsion profiles (red) are not available in the ACC solution. **c** and **d** show the tilts and torsion profiles of the ACC + GYRO solutions and **e** and **f** for the INTEG solutions. In **c** and **e** zoomed-in views of the tilts and torsion profiles are provided, which show that sinusoidal signatures of the M1 tilts and torsion are recovered in both solutions. **d** and **f** show the tilts and torsion profiles of the ACC + GYRO and INTEG solutions obtained with M2

solution. Contrary to the ACC results, the ACC+GYRO solution does not seem to be much affected by the initial misorientation and the displacement errors of horizontal and vertical components are approximately of the same level as the M1 case in terms of displacement, while for velocity the RMS errors of ACC+GYRO are increased by more than 50%. To process the M2 data with the INTEG method, leveling and gyrocompassing are conducted first to obtain initial values of the state variables for tilts and torsion as discussed in Sect. "Methods". The horizontal accuracy of the INTEG displacements becomes worse by approximately 34% than its counterpart in Fig. 2 while the vertical accuracy of INTEG is unexpectedly improved by 78%. In comparison, the horizontal accuracy of ACC is severely degraded by 506% and for ACC+GYRO the accuracy is slightly decreased by 0.3%. The error PSD of vertical displacement of ACC+GYRO becomes somewhat noisier in the frequency range near and above 1 Hz and the error PSD of vertical displacement of INTEG is also increased in the upper frequency band. Unlike the previous results, the ACC response functions in Fig. 3d extend into the very low frequency band, e.g., below 0.1 Hz, particularly for the horizontal components, while the ACC+GYRO response functions seem comparable to the previous results. This difference may be due to the artifacts observed in the displacement waveforms.

In order to examine the accuracy of estimated tilts and torsion from the individual methods, each tilts and torsion solution is plotted and analyzed as shown in Fig. 4. The upper panel of Fig. 4 shows the tilts and torsion obtained from M1 and those obtained from M2 are shown in the lower panel of Fig. 4. As described in Eq. (11), torsion cannot be measured by strong-motion accelerometers alone and thus torsion estimates are provided only for the ACC+GYRO and INTEG solutions. The tilts of the ACC solution are estimated using the data in the first 5-s period with Eq. (11) and held fixed to the values afterwards. It can be observed in Fig. 4a that the

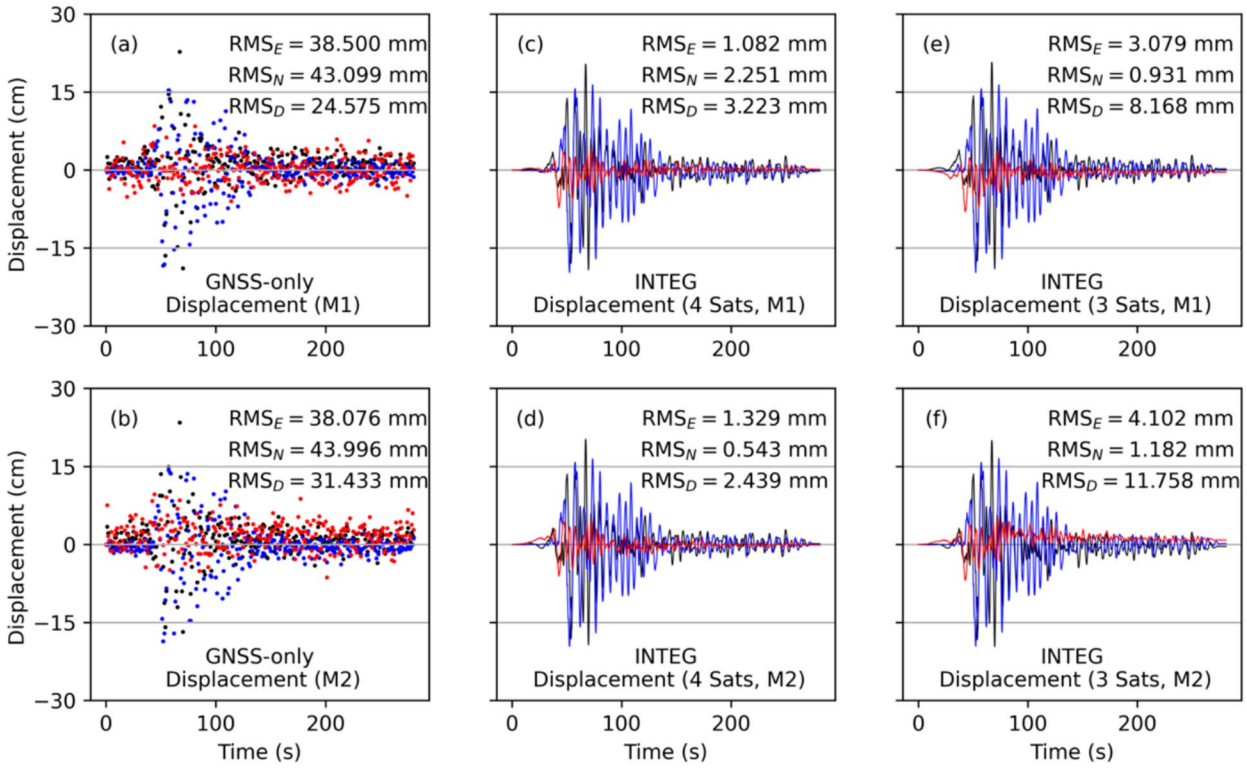

Fig. 5 Displacement profiles obtained by processing the recordings of the El Mayor-Cucapah earthquake with the M1 model (shown in upper panel) and the M2 model (lower panel). Refer to Fig. 2 for the acronyms and symbols. **a** and **b** show 1-Hz, GNSS-derived displacement solutions for the M1 and M2 cases, respectively. **c** and **d** show the displacement waveforms of the 200-Hz, INTEG solutions for the M1 and M2 when the number of tracking satellites is set to four, and similarly **e** and **f** show the INTEG displacement solutions with the number of satellites changed to three

RMS errors of the tilts and torsion estimates of ACC are at the level of 0.01–0.02 degrees, which is mainly attributed to the fact that the ACC solution does not retrieve the sinusoidal tilts of M1. As can be seen in Fig. 4c and e, the ACC+GYRO and INTEG solutions recover the sinusoidal signatures and the RMS error of the torsion profiles of INTEG is somewhat higher than that of the ACC+GYRO solution. This seems to be due to the existence of the residual errors in the torsion profile of INTEG. Recalling Eqs. (5) and (8), the integration filter observes the torsion not directly but indirectly, by experiencing the effects of the torsion, that is, the growth of the velocity errors. Obviously, such growth can be caused by other sources as well. Thus a certain level of horizontal motion and rotation is needed for the integration filter to better observe the effect of the torsion and separate it from those generated by the other sources. This requirement may be rather difficult to be met sufficiently for the strong-motion accelerometers, which are installed on a static instrumentation base. Note that the RMS tilts errors of INTEG are less than that of the torsion at least by an order of magnitude. For the results obtained with M2, the RMS errors of the tilts profiles of the ACC solution are almost the same as the initial misorientation applied (i.e., 0.7 and 0.5 degrees) as seen in (b). The RMS tilts and torsion errors of ACC+GYRO are increased significantly compared to the corresponding M1 results and the RMS value of the torsion profile of ACC+GYRO is somewhat greater than that of the INTEG counterpart. This seems to be due to increased error in determining torsional angle using the gyrocompassing technique. Note that the RMS tilts errors of ACC+GYRO are greater than those of INTEG as well.

Focusing on the characteristics of the INTEG solutions, Fig. 5 shows the displacement waveforms of GNSS-only solutions as well as those of the integrated solutions obtained by changing the number of tracking GNSS satellites. (a) and (b) show the 1-Hz, GNSS-derived displacement solutions obtained from processing the M1 and M2 data. Note that the M2 data used here contain not the initial misorientation but the velocity-dependent tilts and torsion profiles only. (c) and (d) show 200-Hz, INTEG displacement waveforms obtained with M1 where the number of satellites is changed to four and

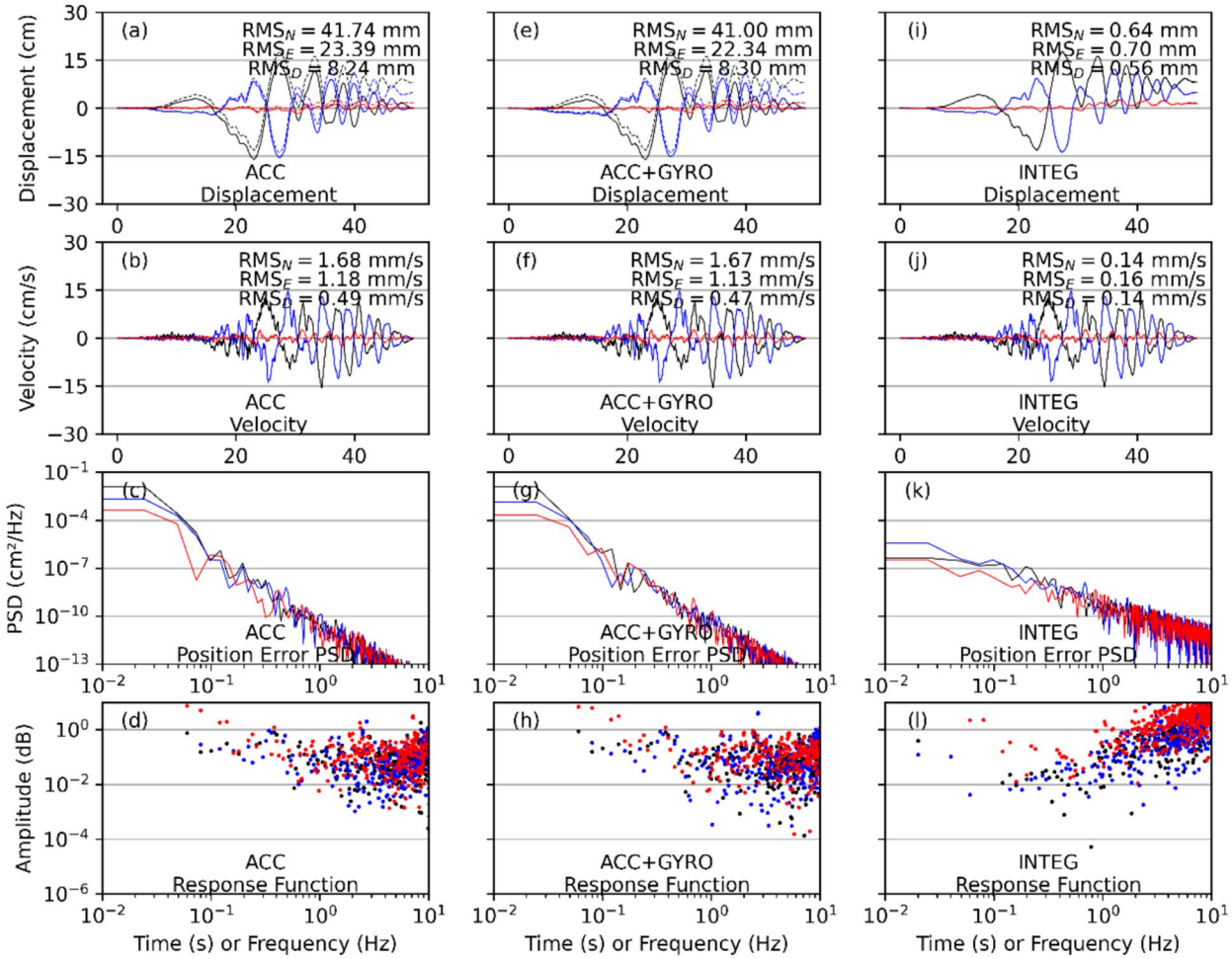

Fig. 6 Results obtained by processing the recordings of the Hector Mine earthquake where the velocity profiles are modified to generate permanent displacements together with tilts and torsion profiles that are proportional to velocity profiles and no initial orientation errors applied. Refer to Fig. 2 for the acronyms and symbols. Panels **a**, **b**, **c** and **d** show displacements, velocities, PSD of position errors, and displacement response functions obtained by the ACC method, respectively. Similarly, panels **e**, **f**, **g**, **h** correspond to the ACC + GYRO method, and panels **i**, **j**, **k**, **l** to the INTEG method. As can be seen in **a** and **e**, the RMS errors of both ACC and ACC +GYRO are increased significantly compared to the previous cases, which is due to failure of both methods to recover the permanent ground deformation. In contrast, the INTEG solution in **i** successfully recovers the permanent displacements successfully in all three components. In **k** the error PSD of the INTEG shows a higher level of variations in a frequency band greater than 1 Hz compared to the El Mayor-Cucapah case. The response functions of all three methods show amplification in vertical displacement (red) for frequencies around or below 0.1 Hz

three, respectively, and similarly (e) and (f) for the M2 counterparts with the same output rate and the numbers of the satellites. As shown in (a) and (b) the RMS errors of the GNSS-only displacement solutions are at the level of 3–4 cm for both M1 and M2, which is comparable to that of nominal PPP solutions and not overly optimistic. Comparing (c) and (e) with Fig. 2i, the RMS errors of the INTEG displacement solutions for M1 are increased with the decrement of the number of satellites, as expected. It is noted that the standard GNSS positioning is not possible when the number of tracking satellites is less than four. The degradation in accuracy is more pronounced in vertical displacement and this seems to be due to poor observational geometry caused by insufficient number of data, leading to the increment of postseismic or residual errors of INTEG vertical displacements. Unlike the M1 case, horizontal displacements of INTEG does not degrade for the M2 case when the number of satellites is set to four while for vertical INTEG displacement solution the RMS error is severely increased compared to Fig. 3i. By changing the number of tracking satellites to three for the M2 case, all three components of the INTEG displacement solutions become worse, at least by 118%. Again the greatest RMS error is with the vertical component and it can be observed from Fig. 5f that the residual errors in vertical displacement persist through

the time span, spanning approximately from 85 s to the end of the data.

In order to further validate the integration strategy using different sets of seismic data, the recordings of two more actual earthquake events are processed and analyzed, which are those of the Hector Mine and the Northridge earthquakes.

Figure 6 shows the results obtained by processing the accelerometer recording from the San Bernardino—Fire Station #10 station during the 1999 Mw 7.1 Hector Mine earthquake with the same three methods. Using the M2 model in the El Mayor-Cucapah case, the torsion and tilts are given in terms of velocity profiles. However, the initial orientation errors are not imposed and the velocity profiles are further modified in such a way that permanent ground deformation occurs in three components when the individual velocity components reach their peaks, which results in non-zero postseismic displacements. This case is representative of the situation where baseline offsets are caused by two mechanisms, e.g., one by tilts and torsion and the other by velocity pulses (Spencer et al. 2000; Emore et al. 2007). For the baseline offsets caused by mechanisms other than local ground rotations, gyroscopes do not directly sense the effects of the offsets. The recordings span for 50 s at sampling frequency of 200 Hz and peak velocities occur at the time of 34.5, 28.8 and 37.9 s for north, east and vertical directions, respectively. The magnitudes of the north, east and vertical permanent displacements are 7.9, 4.7 and 1.6 cm, respectively, and the parameters of the baseline correction for the ACC and ACC + GYRO solutions were newly searched. Consequently, the order of the detrending polynomial was changed to unity and the corner frequency of the high-pass filter was set to 0.001 Hz. For the INTEG solution, on the contrary, the parameters used in the previous experiments were kept the same, maintaining objectivity in data processing.

As shown in Fig. 6, the RMS errors of both ACC and ACC + GYRO are increased significantly compared to the El Mayor-Cucapah case. Differences in position error between the two are minimal, although the horizontal errors of ACC + GYRO are slightly better than those of ACC. This is most likely due to failure of both methods to retrieve the permanent ground deformation accurately as both solutions converge to zero at the end of time span as shown in Fig. 6a and e, which results in the greater RMS errors in all three components. It can be observed in Fig. 6a and e that the horizontal component of the ACC and ACC + GYRO solutions are deviated from the truth waveforms soon after the initial epoch of the data. This is due to the tilt errors which is a scaled version of the velocity forms, are applied from the moment the shaking starts. It may be possible to further reduce the RMS errors using different baseline correction methods (Trifunac 1971; Graizer 1979; Boore et al. 2005), although there is no guarantee that optimal baseline correction parameters selected for one data set would work for another set as well. As shown in the last few seconds of the time span in Fig. 6i, the INTEG solution recovers the permanent displacements in all three components. For PSD of the position errors, frequency spectra of the INTEG position errors show a higher level of fluctuations in a frequency band greater than 1 Hz, particularly at integer multiples of 1 Hz while the PSD plots of ACC and ACC + GYRO do not show much difference between each other as expected from the displacement results. Regarding the response functions of the three methods, all three extends into the low-frequency band below 0.1 Hz. For vertical displacement, the response functions of the three methods show amplification in frequencies below 0.1 Hz. The amplification is more pronounced for the ACC and ACC + GYRO methods and less so for the INTEG method, as shown in Fig. 6d, h and l.

Finally, Fig. 7 shows results obtained by processing the accelerometer recordings of the Jensen Filter Plant Generator Building station during the 1994 Mw 6.7 Northridge earthquake. Similar to the Hector Mine case, velocity profiles are modified to yield permanent displacements with tilts and torsion proportional to velocity profiles with no initial orientation errors applied. The recordings span for about 29 s and peak velocities occur at the time of 3.2, 6.5 and 3.9 s, respectively, which are relatively earlier compared to those of the Hector Mine case. This leads to increased portion of coseismic permanent displacements occupied in the entire time span. The order of the detrending polynomial for baseline correction was changed to three, which was selected from a one parameter search on the optimal order of the detrending polynomial by fixing the corner frequency. The magnitudes of the permanent displacements in north, east and vertical components are 8.0, 5.0 and 1.9 cm, respectively.

As can be observed in Fig. 7a and e, the RMS position errors of the ACC and ACC + GYRO solutions are greatly increased compared to the Hector Mine case, which is most likely due to the extended period of permanent displacements in time span. There is no substantial difference between ACC and ACC + GYRO solutions. The RMS errors of both solutions induced by failure to recover the permanent displacements seem to overshadow the other errors and thus obscure the difference between the ACC and ACC + GYRO solutions, which results in almost the same level of RMS errors between the two solutions. As shown in Fig. 7i, the INTEG solution maintains the similar level of position accuracy in all three components as those from the El Mayor-Cucapah case, although the RMS values are somewhat increased

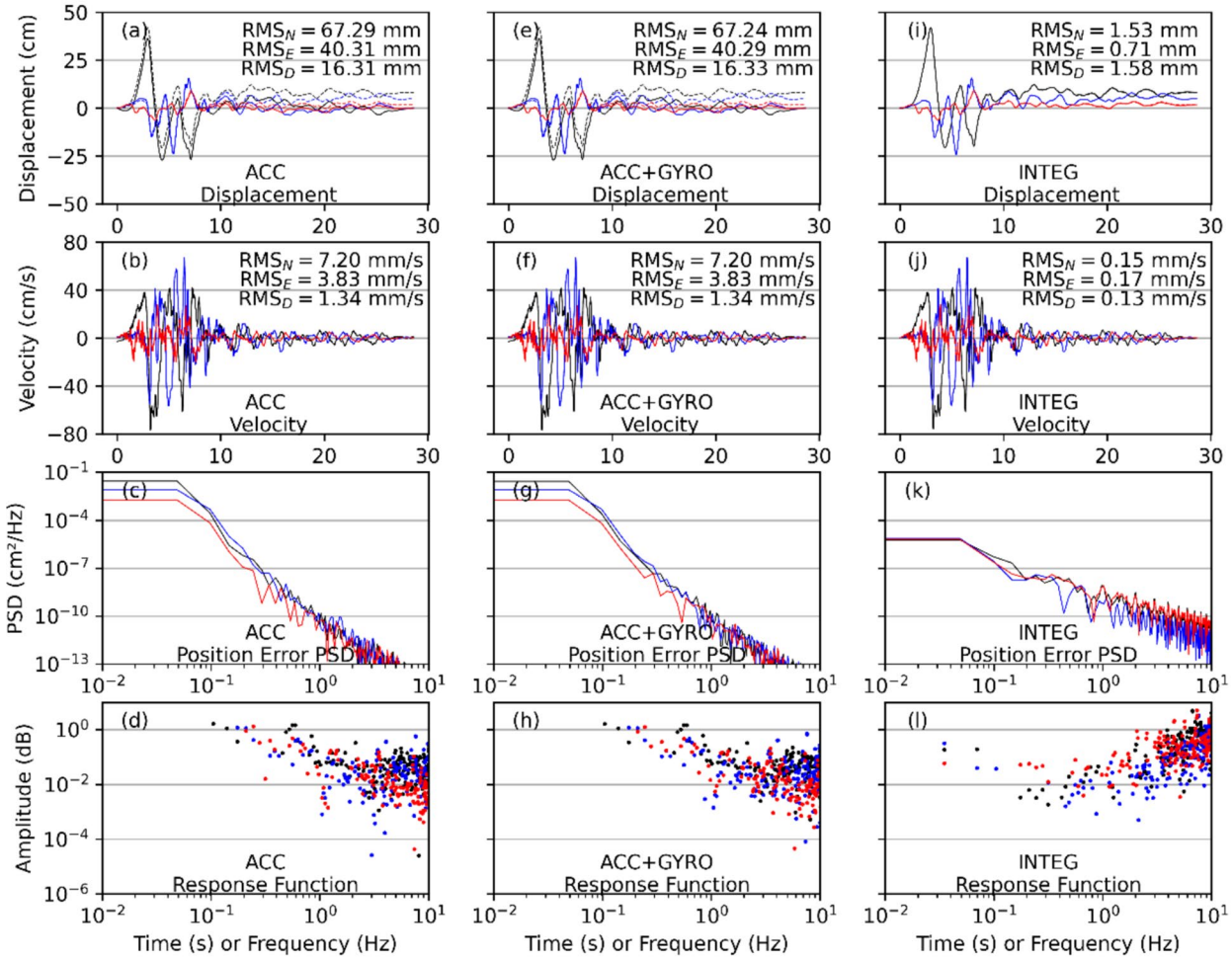

Fig. 7 Results obtained by processing the recordings of the Northridge Earthquake where tilts and torsion proportional to velocity profiles are applied with no initial orientation errors. The velocity profiles are modified in the same way as in Hector Mine case, but the duration of permanent displacements is extended by 50% in an average sense. See Fig. 2 for the acronyms and symbols. Panels **a**, **b**, **c** and **d** show displacements, velocities, PSD of position errors, and displacement response functions obtained by the ACC method, respectively. Similarly, panels **e**, **f**, **g**, **h** correspond to the ACC + GYRO method, and panels **i**, **j**, **k**, **l** to the INTEG method. **a** and **e** show that the RMS errors of the displacement waveforms of ACC and ACC + GYRO are almost the same while i shows that the INTEG solution is more accurate than those from ACC and ACC + GYRO by at least an order of magnitude. Similar to the Hector Mine case permanent deformation is recovered by the INTEG method as shown in **i**. In **k** the INTEG displacement solution shows a better performance in the frequency range from 0.01 to 0.7 Hz, but in the upper band the INTEG solution becomes noisier than those from ACC + GYRO. The INTEG method's response function extends further into the low-frequency band below 0.1 Hz compared to those of ACC and ACC + GYRO. This extension is linked to the INTEG method's ability to capture permanent displacements, which are associated with very low frequencies.

compared to the Hector Mine case. For the PSD plot of position errors, the PSD of the ACC and ACC+GYRO solutions decreases almost linearly in the frequency band above 0.05 Hz. The INTEG solution shows better performance in the frequency range from 0.01 to 0.7 Hz than the two solutions, but in the upper band the INTEG solution becomes noisier, which is likely due to the 1-Hz update of the states from the EKF integration filter. The response functions for ACC and ACC+GYRO show a cutoff around 0.1 Hz, indicating that they do not extend into lower frequencies in this case. In contrast, the INTEG method's response function extends down to 0.03 Hz, capturing a broader frequency range, particularly in the very low-frequency band. This is linked to the capture of permanent displacements associated with very low frequencies.

Conclusions

We investigate the potential benefits of tightly integrating gyroscopes and GNSS with strong-motion accelerometers by comparing with the traditional methods when the

sensors are affected by rotation and tilting motions of the ground.

Based on the comparisons between the ACC and ACC+GYRO solutions, the added value of gyroscopes alone lies mainly in the improvement of the horizontal accuracy of the displacement profiles for baseline offsets induced by the tilts and torsion. This suggests that the gyroscopes are more useful for mitigating tilting motions of the ground than torsion and if only two gyroscopes should be installed in a seismic station, for instance for cost reduction, they would be better used on the north and east axes and if any, a cheaper, lower-grade gyroscope could be used for the vertical axis. However, for the baseline offsets induced by a mechanism other than tilts of the ground, the addition of gyroscopes does not appear to provide any meaningful improvement compared to accelerometer-only instrumentation.

Based on the results obtained from the El Mayor-Cucapah case, the Hector Mine and the Northridge cases, we conclude that integrating GNSS with the strong-motion accelerometers and gyroscopes improve the accuracy of resulting displacement waveforms in all three components, compared to the traditional methods based on accelerometers-only and inertial (accelerometers and gyroscopes) instruments at least by 50% and in some cases by one or two orders of magnitude more, especially for the recordings with permanent ground deformation.

To obtain realistic displacement waveforms using the ACC and ACC+GYRO methods, baseline corrections must be applied to remove low-frequency or long-period components of the velocity waveforms. Since low-frequency components include those associated with permanent displacements, recovering permanent displacements using these methods becomes challenging, which results in a significant increase in the RMS errors in the Hector Mine and Northridge cases. In contrast, the INTEG method has proven particularly effective in recovering permanent displacements, with the integration filter settings remaining consistent across all cases. This ability can be attributed partly to the fact that the INTEG method does not suffer the loss of low-frequency components caused by baseline correction and also partly to its incorporation of GNSS measurements, which directly sense permanent displacements.

Specifically, the INTEG method demonstrates a significant advantage in capturing very low-frequency signals, particularly those below 0.1 Hz, which are essential for accurately estimating permanent displacements in seismic events. Unlike the ACC and ACC+GYRO methods, which often have limitations in the low-frequency range, the INTEG method consistently extends further into this band, offering a more comprehensive view of seismic motion. This enhanced capability is critical for modeling and analyzing long-duration seismic events, where low-frequency components are often the primary contributors to permanent displacements. Consequently, the INTEG method serves as a valuable tool for improving the precision of seismic displacement measurements, particularly in scenarios where capturing low-frequency signals is particularly critical.

In the synthetic case studies, we assumed that the distance between inertial instruments and GNSS antenna remains fixed during shaking events and the distance was utilized to translate the position and velocity vectors of the origin of the body frame, i.e., the inertial instruments, to the phase center of the GNSS antenna. This may not be the case in reality. If the magnitude of the distance varies during seismic events or if earthquake-induced relative motion occurs between the inertial instruments and the GNSS antenna—such as when GNSS antennas are mounted on relatively flexible structures while inertial sensors are installed on rigid foundations—the distance should be estimated within the integration filter. This is equivalent to treating the distance vector as an additional state variable. As described in Eq. (9), the translation of the position and velocity vectors between the strong-motion accelerometers and the GNSS antenna is expressed in terms of the distance vector and the Direction Cosine Matrix (DCM) for the body-to-ECEF transformation, which is used to compute the corresponding measurement partials. Modifying the integration filter primarily involves augmenting the filter state vector to include the distance vector and updating the measurement dynamics and the time update of the EKF to estimate the distance vector.

Acknowledgements
This work was funded by the Korea Meteorological Administration Research and Development Program under Grant KMI2018-02710. Strong motion accelerometer recordings used in this paper were provided by the PEER Ground Motion Database of the Pacific Earthquake Research Center.

Author contributions
SL, CC and SY conceptualized the idea of the research and did analytical work. Data analysis was performed by SL and JK. BT provided critical feedback and helped shaping the research.

Funding
This work was funded by the Korea Meteorological Administration Research and Development Program under Grant KMI2018-02710.

Availability of data and materials
No datasets were generated or analysed during the current study.

Declarations

Competing interests
The authors declare no competing interests.

Received: 11 June 2024 Accepted: 27 March 2025
Published online: 29 April 2025

References

Bernauer M, Fichtner A, Igel H (2014) Reducing nonuniqueness in finite source inversion using rotational ground motions. J Geophys Res Solid Earth 119:4860–4875. https://doi.org/10.1002/2014JB011042

Blewitt G, Hammond WC, Kreemer C, Plag HP, Stein S, Okal E (2009) GPS for real-time earthquake source determination and tsunami warning systems. J Geod 83(3):335–343. https://doi.org/10.1007/s00190-008-0262-5

Bock Y, Melgar D, Crowell BW (2011) Real-time strong-motion broadband displacements from collocated GPS and accelerometers. Bull Seismol Soc Am 101(6):2904–2925. https://doi.org/10.1785/0120110007

Boore DM, Joyner WB, Oliver AA, Page RA (1980) Peak acceleration, velocity, and displacement from strong-motion records. Bull Seismol Soc Am 70:305–321. https://doi.org/10.1785/BSSA0700010305

Boore DM (2003) Analog-to-digital conversion as a source of drifts in displacements derived from digital recordings of ground acceleration. Bull Seismol Soc Am 93(5):2017–2024. https://doi.org/10.1785/0120020239

Boore DM, Bommer JJ (2005) Processing of strong-motion accelerograms: needs, options, and consequences. Soil Dyn Earthquake Eng 25:93–115. https://doi.org/10.1016/j.soildyn.2004.10.007

Bouchon M, Aki K (1982) Strain, tilt, and rotation associated with strong ground motion in the vicinity of earthquake faults. Bull Seismol Soc Am 72:1717–1738. https://doi.org/10.1785/BSSA0720051717

Brown RG, Hwang PYC (1997) Introduction to Random Signals and Applied Kalman Filtering, 3rd edn. Wiley, New York

Colosimo GM, Crespi M, Mazzoni A (2011) Real-time GPS seismology with a stand-alone receiver: a preliminary feasibility demonstration. J Geophys Res 116:B11302. https://doi.org/10.1029/2010JB007941

Dai JS (2015) Euler-Rodrigues formula variations, quaternion conjugation and intrinsic connections. Mech Mach Theory 92:144–152. https://doi.org/10.1016/j.mechmachtheory.2015.03.004

Durrant-Whyte HF (2016) Sensor models and multisensor integration. The Int J Robotics Res 7(6):97–113. https://doi.org/10.1177/027836498800700608

Emore G, Haase JS, Choi K, Larson KM, Yamagiwa A (2007) Recovering seismic displacements through combined use of 1-Hz GPS and strong-motion accelerometers. Bull Seismol Soc Am 97:357–378. https://doi.org/10.1785/0120060153

Farrell JL (2007) GNSS aided navigation and tracking: inertially augmented or autonomous. American Literary Press, Baltimore MD

Gelb A (ed) (1974) Applied optimal estimation. MIT Press, Cambridge, MA

Greenspan RL (1996) GPS and inertial integration. In: Parkinson BW, Spilker JJ (eds) Global positioning system: theory and applications. AIAA, Washington, DC

Grewal MS, Weill LR, Andrews AP (2007) Global positioning systems, inertial navigation, and integration, 2nd edn. Wiley, New York

Graizer VM (1979) Determination of the true displacement of the ground from strong-motion records. Izvestya USSR Acad Sci Phys Solid Earth 15(12):875–885

Graizer VM (2006) Tilts in strong ground motion. Bull Seismol Soc Am 96:2090–2102. https://doi.org/10.1785/0120060065

Hartzell SH, Heaton TH (1983) Inversion of strong ground motion and teleseismic waveform data for the fault rupture history of the 1979 imperial-valley, California, earthquake. Bull Seismol Soc Am 73:1553–1583. https://doi.org/10.1785/BSSA07306A1553

Igel H, Schreiber U, Flaws A, Schuberth B, Velikoseltsev A, Cochard A (2005) Rotational motions induced by the M8.1 Tokachi-oki earthquake, September 25, 2003. Geophys Res Lett 32(8):L08309. https://doi.org/10.1029/2004GL022336

Igel H, Cochard A, Wassermann J, Flaws A, Schreiber U, Velikoseltsev A, Pham ND (2007) Broad-band observations of earthquake-induced rotational ground motions. Geophys J Int 168(1):182–196. https://doi.org/10.1111/j.1365-246X.2006.03146.x

Jekeli C (2000) Inertial navigation systems with geodetic applications, de Gruyter. Berlin, Germany. https://doi.org/10.1515/9783110800234

Kramer SL (1996) Geotechnical earthquake engineering. Prentice-Hall, New Jersey

Lee SW, Kouba J, Schutz BE, Kim DH, Lee YJ (2013) Monitoring precipitable water vapor in real-time using global navigation satellite systems. J Geod 87:923–934

Lee SW, Yun SH, Kim DH, Lee D, Lee YJ, Schutz BE (2015) Real-time volcano monitoring using GNSS single-frequency receivers. J Geophys Res Solid Earth 120:8551–8569. https://doi.org/10.1007/s00190-013-0655-y

Lee WHK, Celebi M, Todorovska MI, Igel H (2009) Introduction to the special issue on rotational seismology and engineering applications. Bull Seismol Soc Am 99(2B):945–957. https://doi.org/10.1785/0120080344

Nigbor RL (1994) Six-degree-of-freedom ground motion measurement. Bull Seismol Soc Am 84(5):1665–1669. https://doi.org/10.1785/BSSA0840051665

Ohta Y, Kobayashi T, Tsushima H, Miura S, Hino R, Takasu T, Umino N (2012) Quasi real-time fault model estimation for near-field tsunami forecasting base on RTK-GPS analysis: Application to the 2011 Tohoku-Oki earthquake (Mw 9.0). J Geophys Res 117:B02311. https://doi.org/10.1029/2011JB008750

Rogers RM (2000) Applied Mathematics in Integrated Navigation Systems. AIAA, Reston, VA

Shakal AF, Huang M, Graizer VM (2004) CSMIP strong-motion data processing. Paper presented at Invited Workshop on Strong-Motion Record Processing, Consortium of Organizations for Strong-Motion Observation Systems (COSMOS), Richmond, California, 26–27 May 2004

Spencer BF, Johnson E, Ramallo J (2000) "Smart" isolation for seismic control. JSME Int J Ser C 43:704–711. https://doi.org/10.1299/jsmec.43.704

Symans MD, Madden GJ, Wongprasert N (1999) Semi-active hybrid isolation systems: addressing the limitations of passive isolation systems, In: Proceedings of Structures Congress, ASCE, New Orleans, LA, 1999

Takeo M (1998) Ground rotational motions recorded in near-source region of earthquakes. Geophys Res Lett 25(6):789–792. https://doi.org/10.1029/98GL00511

Tapley BD, Schutz BE, Born GH (2004) Statistical orbit determination. Elsevier Academic Press, Amsterdam

Titterton DH, Weston JL (2004) Strapdown inertial navigation technology, 2nd edn. Stevenage, UK

Trifunac MD (1971) Zero baseline correction of strong-motion accelerograms. Bull Seismol Soc Am 61:1201–1211. https://doi.org/10.1785/BSSA0610051201

Trifunac MD (1982) A note on rotational components of earthquake motions for incident body waves. Soil Dyn Earthquake Eng 1:11–19. https://doi.org/10.1016/0261-7277(82)90009-2

Trifunac MD, Todorovska MI (2001) A note on the usable dynamic range of accelerographs recording translation. Soil Dyn Earthquake Eng 21:275–286. https://doi.org/10.1016/S0267-7261(01)00014-8

Trifunac MD (2009) Rotations in structural response. Bull Seismol Soc Am 2B:968–979. https://doi.org/10.1785/0120080068

Wald DJ, Heaton TH (1994) Spatial and temporal distribution of slip for the 1992 landers California, earthquake. Bull Seismol Soc Am 84:668–691. https://doi.org/10.1785/BSSA0840030668

Wei M, Schwarz KP (1990) A strapdown inertial algorithm using an earth-fixed cartesian frame. Navigation 37(2):153–167. https://doi.org/10.1002/j.2161-4296.1990.tb01544.x

Publisher's Note